Vapor-gap membranes for highly selective osmotically driven desalination

Jongho Lee[a,c,*], Anthony P. Straub[b,c], Menachem Elimelech[c]

[a] Department of Civil Engineering, University of British Columbia, Vancouver, BC, Canada V6T 1Z4
[b] Department of Materials Science and Engineering, Massachusetts Institute of Technology, Cambridge, MA 02139, United States
[c] Department of Chemical and Environmental Engineering, Yale University, New Haven, CT 06520-8286, United States

A B S T R A C T

In this study, we demonstrate nanostructured osmosis membranes that employ vapor-phase water transport to simultaneously achieve high rejection of solutes and a high permeability. The membranes consist of a hydrophobic, thermally conductive silica nanoparticle (SiNP) layer with tunable thickness supported by a hydrophilic track-etched membrane. The membrane permeability for water vapor is 1–2 orders of magnitude higher than hydrophobic microporous membranes used for osmotic distillation. This permeability is only mildly lower (~ 3 times) than the equivalent water permeability of typical forward osmosis (FO) membranes. We also demonstrate the high selectivity of the SiNP membrane via urea permeation tests, where this membrane exhibits a 2–3 orders of magnitude lower urea permeability coefficient than a thin-film composite (TFC) FO membrane. Further measurements and theoretical analysis using the dusty-gas model suggest that membranes with a smaller SiNP layer thickness are capable of having comparable water fluxes to TFC FO membranes while maintaining higher selectivity. Our work demonstrates that thin, hydrophobic nanostructured membranes composed of thermally conductive materials have a great potential to significantly extend the applications of osmosis-driven processes to treat challenging water sources.

1. Introduction

Osmotically driven membrane processes, which utilize the same principle of osmosis prevalent in biological systems, employ a semipermeable membrane placed between two solutions of different solute concentrations: a feed water of low concentration and a draw solution of high concentration. The chemical potential difference between the two solutions drives a water flux through the membrane from the feed to the draw solution, while solute molecules are rejected by the membrane. Osmotically driven processes offer several advantages, including low fouling susceptibility, the ability to treat high salinity source waters, and low energy cost if waste heat is used for draw solution recovery [1–3].

The most notable technology for osmotically driven separations is forward osmosis (FO), a membrane process that extracts water via liquid-phase osmotic flow across a semi-permeable membrane. Polyamide-based thin-film composite (TFC) membranes are the state-of-the-art salt-rejecting membranes and are therefore widely adapted for FO [2,3]. However, all polymer-based membranes suffer from an inherent limitation on their achievable permeability and selectivity, so any further increases in the selectivity of current polymer membranes cannot be achieved without sacrificing water permeability. In addition,

TFC membranes cannot adequately reject small, neutrally charged solutes such as urea, boron, and other emerging trace organic contaminants [4–6].

Alternatively, osmotically driven separation employing hydrophobic porous membranes (i.e., vapor-gap membranes), also called osmotic distillation (OD), can potentially enable near-complete rejection of non-volatile solutes. The hydrophobicity of vapor gap membranes leads to the formation of an air gap between the draw and feed streams. For water to be transported through the membrane, it must evaporate on one side of the liquid-vapor interface and then condense on the opposite side [7]. Unlike polyamide membranes, which are subject to a permeability-selectivity trade-off [8,9], the use of this phase-change process allows for a decoupling of permeability and selectivity. Desalination with defect-free hydrophobic membranes guarantees high rejection of non-volatile solutes in addition to near complete rejection of salt, regardless of the water permeability. Therefore, it is in principle possible to simultaneously achieve high permeability and solute rejection, even for neutral species (such as boron and urea), if a thin hydrophobic membrane is employed.

While the potential of vapor-gap membranes is promising for osmotically driven processes, in practice the achievable water permeability of the membrane has been far too low for practical operation

---

Nomenclature

$\bar{a}$	Average radius of SiNPs (m)
a_{eff}	Effective pore radius of SiNP layer (m)
A_v	Vapor permeability coefficient (kg m^{-2} s^{-1} Pa^{-1}). Presented in kg m^{-2} h^{-1} Pa^{-1} in Figs. 5 and 6.
B_0	Viscous permeability (m^2)
B_{urea}	Urea permeability coefficient (m s^{-1})
C	Solute molar concentration (mol m^{-3})
C_{urea}	Urea molar concentration (mol m^{-3})
D_{ij}	Maxwell-Stefan diffusion coefficient of species i in species j (m^2 s^{-1})
D_{iM}	Knudsen diffusion coefficient of species i (m^2 s^{-1})
D_{ij}^e	Effective Maxwell-Stefan diffusion coefficient of species i in species j (m^2 s^{-1})
D_{iM}^e	Effective Knudsen diffusion coefficient of species i (m^2 s^{-1})
D_{wa}	Maxwell-Stefan diffusion coefficient of water in air (m^2 s^{-1})
D_{wM}	Knudsen diffusion coefficient of water (m^2 s^{-1})
J_w	Mass flux of water vapor across the membrane (kg m^{-2} s^{-1}). Presented in kg m^{-2} h^{-1} in Figs. 4–6, and Table 1.
Kn	Knudsen number
k_{eff}	Effective thermal conductivity of SiNP layer
k_s	Thermal conductivity of silica (= 1.4 W m^{-1} K^{-1})
ΔL	Latent heat of water (= 2.26 × 10^6 J kg^{-1})
l	SiNP layer thickness (m)
M_w	Molar mass of water (= 1.8 × 10^{-2} kg mol^{-1})
N_i	Molar flux of species i (mol m^{-2} s^{-1})
N_{urea}	Molar flux of urea (mol m^{-2} s^{-1})
p_0	Vapor pressure of pure water (Pa)
p_D	Partial vapor pressure on draw solution side (Pa)
p_F	Partial vapor pressure on feed solution side (Pa)
p_t	Total pressure in membrane (Pa)
P	Hydraulic pressure (Pa)
R_g	Universal gas constant (= 8.31 J mol^{-1} K^{-1})
T	Temperature (K)
V_m	Molar volume of liquid-phase water (= 1.8 × 10^{-5} m^3 mol^{-1})
x_i	Mole fraction of species i

Greek letters

α	Molecular-to-Knudsen diffusion coefficient ratio
ε	Membrane porosity
τ	Tortuosity factor
η	Dynamic viscosity (Pa s)
Π	Osmotic pressure (Pa)

Superscripts and subscripts

a	Air
D	Draw solution
F	Feed solution
w	Water vapor

Abbreviations

FO	Forward osmosis
MD	Membrane distillation
OD	Osmotic distillation
PCTE	Polycarbonate track-etched
SiNP	Silica nanoparticle
TFC	Thin-film composite

[10–15]. The low water flux can be attributed to the relatively large thickness of current hydrophobic membranes (~ 100 µm), which results in high transport resistance across the air gap and thus a low permeability for water vapor. Current commercial hydrophobic membranes are also commonly made of polymeric materials of low thermal conductivity. A low thermal conductance across the membrane induces a severe temperature polarization, which occurs because the transported water vapor cools the feed side as it evaporates and heats the permeate after it condenses. This effect reduces the partial vapor pressure difference at the air-liquid interface as compared to that achievable at an isothermal condition, decreasing the water flux across the membrane. Due to the unfavorable membrane properties (i.e., low permeability and thermal conductivity), reported water fluxes with vapor-gap membranes are far lower (2–4 orders of magnitude) than those with polyamide membranes when the same osmotic pressure difference is used in osmotically driven processes [10–15]. As a result, vapor-gap membranes have only found niche applications in areas such as food processing [16].

An ideal vapor-gap membrane in OD should be thin (< 1 µm) and thermally conductive to allow for a high permeability and a near isothermal condition. It must also be robust and defect-free to prevent wetting and leakage of contaminants across the membrane. To meet the requirements of high performance OD membranes, a novel fabrication method is necessary that allows for simple tunability of the hydrophobic layer thickness, enabling osmotically driven processes to simultaneously achieve high selectivity and high water permeability.

In this work, we develop a vapor-gap membrane with a sub-micrometer thick and thermally conductive nanoparticle layer for highly selective and permeable osmotically driven separation. We construct a hydrophobic layer of tunable thickness using fluorosilane-coated silica nanoparticles (SiNPs) deposited on a hydrophilic polycarbonate track-

etched (PCTE) membrane. Vapor-phase water transport through the membrane and high salt rejection are demonstrated in osmotic distillation experiments. A theoretical analysis is used to further investigate the potential for high flux membranes. Finally, we perform urea permeation tests to demonstrate the rejection performance against small neutral molecules. The fabricated membrane combines the advantages of both hydrophobic distillation membranes (high rejection) and conventional TFC membranes (high permeability).

2. Theory

In osmotic distillation, water molecules evaporate from the feed water, move across the hydrophobic membrane, and condense on the draw solution (Fig. 1). Each of these steps introduces resistances to water transport through the membrane. Considering that the typical membrane thickness (1–100 µm) is much larger than the characteristic pore size (0.01–10 µm), the mass transport resistance for vapor transmission inside the membrane is much higher than the resistances associated with the evaporation and the condensation steps [17,18]. The fast evaporation and condensation rates compared to vapor transport in the membrane lead to near vapor-liquid equilibrium on both the feed and draw sides of the membrane. Therefore, as in most cases of membrane distillation (MD), the mass flux in OD is mainly determined by the water vapor transport, driven by a partial vapor pressure gradient inside the hydrophobic membrane.

2.1. Vapor permeability of hydrophobic membranes

Since increased salinity depresses the partial vapor pressure of water, vapor will move from the low-salinity feed side of the membrane to the high-salinity draw side, interacting with other gas molecules (i.e.,
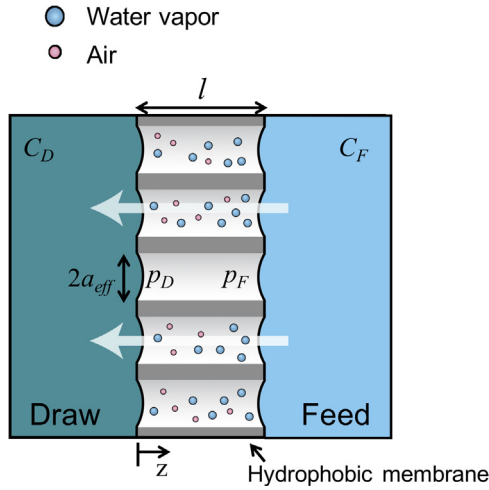
Fig. 1. Schematic illustration of an osmotic distillation process. Water vapor is transported from the feed solution to the draw solution (arrows across the membrane) while air molecules are stagnant in the pores. The draw solute concentration, C_D, is higher than the feed concentration, C_F, resulting in a partial vapor pressure on the draw side of the membrane, p_D, that is lower than the partial vapor pressure on the feed side, p_F. In the schematic, a_{eff} is the effective pore radius, l is the membrane thickness, and z is the perpendicular distance into the membrane from the draw side membrane-solution interface.

air) and the membrane. Transport of a multi-component gas mixture through a porous medium is described by the dusty-gas model, which can be regarded as an extension of the Stefan-Maxwell diffusion model [19–21]. The Stefan-Maxwell model describes the friction forces experienced by gas molecules due to interactions with other molecules (i.e., molecular diffusion) and the impact of external driving forces, such as (electro)chemical potential gradients [21]. The dusty-gas model accounts for the friction from gas molecules interacting with the pore walls (i.e., Knudsen diffusion) by treating the membrane as stagnant gas particles that are uniformly distributed. In addition, the dusty-gas model assumes that diffusive and viscous flows are additive for each gas species. This model was experimentally verified in binary [22] and ternary [23] gas systems for diffusion of inert gases under uniform pressure from the Knudsen to the molecular diffusion regime, and it has been successfully applied for modeling gas transport in various systems, including MD [24–26].

Assuming that water vapor and air behave as ideal gases in the typical operation conditions of OD (pressure of ~ 1 bar, temperatures of 10–60 °C), the generalized Stefan-Maxwell equation combined with the dusty-gas model can delineate mass fluxes of each gas species resulting from Knudsen diffusion, molecular diffusion, and viscous flow, as follows [19,24,27]:

$$\sum_{j=1, j\neq i}^{n} \frac{x_j N_i - x_i N_j}{D_{ij}^e} + \frac{N_i}{D_{iM}^e} = -\frac{p_t}{R_g T}\nabla x_i - \frac{x_i}{R_g T}\left(1 + \frac{B_0 p_t}{\eta D_{iM}^e}\right)\nabla p_t. \tag{1}$$

Here, x_i and N_i are the mole fraction and average molar flux of gas species i, respectively; p_t, R_g, and T are the total pressure, universal gas constant, and absolute temperature, respectively; η is the dynamic viscosity of the gas mixture; B_0 is the viscous permeability of the membrane; z is the perpendicular distance into the membrane from the draw side membrane-solution interface (Fig. 1); D_{ij}^e is the effective molecular diffusion coefficient arising from the interaction between species i and j; and D_{iM}^e is the effective Knudsen diffusion coefficient associated with the interaction of species i with the membrane. D_{ij}^e is commonly expressed as the binary molecular diffusion coefficient (D_{ij}) multiplied by membrane porosity (ε) and divided by membrane tortuosity factor (τ). Similarly, D_{iM}^e is expressed as $(\varepsilon/\tau)D_{iM}$, where D_{iM} is the Knudsen diffusion coefficient for species i [27]. The last term in the parenthesis on the right-hand side of the equation indicates the

contribution from the viscous flow driven by the total pressure gradient.

Several approximations can be made to simplify Eq. (1). First, the constituent gas molecules of air, such as nitrogen and oxygen, are modeled as one species (i.e., air) [18,24,28]. This approximation allows us to treat the gas inside the membrane as a binary mixture of water vapor and air. Second, because of the very small solubility of air in water, air is assumed to be stagnant within the pores. Third, we only consider gas flows in the z direction (Fig. 1). Fourth, we neglect the viscous flow based on comparison of the magnitude of viscous flux and diffusive fluxes (Appendix A). Fifth, we assume a uniform total pressure inside the membrane [18,28]. Finally, we assume that the system is under isothermal condition (uniform temperature) since the temperature difference across the membrane is expected to be less than 0.1 °C based on the balance between latent heat transfer in water vapor and conductive heat transfer through the membrane (Appendix B).

Applying the simplifying approximations and integrating Eq. (1) yields the following expression for the molecular flux of water vapor [28] (see also Appendix A for a detailed derivation):

$$N_w = \frac{\varepsilon D_{wa} p_t}{\tau R_g T l} ln\left[\frac{1 - \frac{p_F}{(1+\alpha)p_t}}{1 - \frac{p_D}{(1+\alpha)p_t}}\right], \tag{2}$$

where p_F and p_D are partial vapor pressures at the feed and draw solution sides, respectively, l is the membrane thickness, and α is the diffusion coefficient of water vapor in air, D_{wa}, divided by the Knudsen diffusion coefficient of water, D_{wM} ($\alpha = D_{wa}/D_{wM}$). A first-order Taylor approximation allows us to obtain a simplified expression for the mass flux of water vapor, J_w:

$$J_w = M_w |N_w| = \frac{\varepsilon D_{wa} M_w}{\tau R_g T l (1 + \alpha)}(p_F - p_D), \tag{3}$$

where M_w is the molar mass of water.

As a characteristic membrane transport parameter, we define the vapor permeability coefficient, A_v, as mass flux per given partial vapor pressure difference:

$$A_v = \frac{J_w}{p_F - p_D} = \frac{\varepsilon D_{wa} M_w}{\tau R_g T l (1 + \alpha)}. \tag{4}$$

Examination of Eq. (4) reveals the structural dependency of the vapor permeability coefficient. The Knudsen diffusion coefficient (D_{wK}) is proportional to effective pore radius (a_{eff}), while the molecular diffusion coefficient (D_{wa}) is independent of pore geometry (see Appendices A and C). As a result, α ($= D_{wa}/D_{wM}$) is inversely proportional to a_{eff}. For large a_{eff} ($\alpha << 1$), molecular diffusion is the dominant vapor transport mechanism. Hence, A_v, and therefore J_w, become inversely proportional to the membrane thickness (l), i.e., $A_v \propto l^{-1}$, and independent of a_{eff}. For small a_{eff} ($\alpha >> 1$), on the other hand, water vapor is transported through the membrane primarily via Knudsen diffusion. In this case, A_v and J_w are inversely proportional to the ratio of the membrane thickness to the effective pore radius, i.e., $A_v \propto (l/a_{eff})^{-1}$. A more detailed discussion is presented in Appendix A.

Although temperature impacts D_{wa} and D_{wM} (and therefore α), A_v demonstrates a very weak temperature dependence, showing less than 1% change over a realistic temperature range of 20–80 °C (Appendix C and Fig. S1). Therefore, A_v is mainly determined by geometric parameters (i.e., l and a_{eff}), and can be used as an intrinsic membrane property of OD membranes, analogous to the water permeability coefficient in FO and MD membranes [28,29].

2.2. Relation between partial vapor pressure and osmotic pressure

Partial vapor pressure is dependent on various parameters, including temperature (T), solute concentration (C), and hydraulic pressure (P). In OD, the concentration-dependence of the partial vapor

pressure drives the water vapor. Also known as the Kohler equation [30], the relation between the vapor pressure of pure water and that of an aqueous solution containing solutes can be written as [17,18]:

$$p(T, C, P) = p_0(T)exp\left[\frac{(P - \Pi)V_m}{R_g T}\right], \tag{5}$$

where V_m is the molar volume of water, P is the hydraulic pressure of the solution (liquid phase), Π is the osmotic pressure due to solutes with concentration of C, and p_0 is the vapor pressure of pure water as a function of T only.

Using a first-order Taylor approximation, we obtain the following relation for the partial vapor pressure difference across the membrane (see Appendix D):

$$p_F - p_D = \frac{\Delta \Pi V_m}{R_g T} p_0(T). \tag{6}$$

This expression indicates that the total partial vapor pressure difference is (i) highly dependent on temperature due to the contribution of the vapor pressure of pure water ($p_0(T)$) and (ii) linearly proportional to the osmotic pressure difference (as will be shown experimentally later).

For the actual calculation of A_v from the experimentally measured water flux, J_w, the partial vapor pressure difference was calculated using the Antoine equation for $p_0(T)$ [24] and using commercial software from OLI Systems (Morris Plains, NJ) to determine the osmotic pressure at a given temperature and draw solution concentration.

3. Materials and methods

3.1. Materials and chemicals

Polycarbonate track-etched membranes (PCTE, WHA800308, nominal pore size of 50 nm, thickness of 7–22 μm), dopamine hydrochloride, tris(hydroxymethyl)aminomethane (Tris, > 99.8%), polyethylenimine (PEI, branched, Mw of ~ 1300 g/mol), ethanol (200 proof), urea, diacetyl monoxime (DAM), thiosemicarbazide (TSC), ferric sulfate hydrate (Fe$_2$(SO$_4$)$_3$, 97%), and sulfuric acid (ACS reagent, 95.0–98.0%) were purchased from Sigma-Aldrich (St. Louis, MO, USA). Silica nanoparticles (SiNPs, Nanoxact, dispersed in water with a concentration of 10 mg/mL, nominal diameter of 100 nm) were obtained from Nanocomposix, Inc. (San Diego, CA, USA). (heptadecafluorotetrahydrodecyl)-triethoxysilane (C$_{16}$H$_{19}$F$_{17}$O$_3$Si, hereafter denoted as FDTES) was purchased from Gelest Inc. (Morrisville, PA, USA). A commercial TFC FO membrane (Hydration Technology Innovations,

Albany, OR, USA) was used as a representative FO membrane for comparison of urea rejection. The transport properties (water permeability and salt permeability coefficients) of this membrane have been reported elsewhere [31]. Samples of polytetrafluoroethylene (PTFE) membranes (PTF020LH0P, nominal pore size of 200 nm, called PTFE 200 hereafter) and PVDF membranes (HVHP14250, nominal pore size of 450 nm, called PVDF 450 hereafter) were received from Pall Corporation (Port Washington, NY, USA) and EMD Millipore (Billerica, MA, USA), respectively. Deionized (DI) water was supplied by a Milli-Q ultrapure water purification system (Millipore, Billerica, MA, USA). Osmotic distillation setup was built by assembling a diffusion cell (Permegear Inc., Hellertown, PA, USA), a glass syringe (Model 725 LT SYR, Hamilton Company, Reno, NV, USA), a peristaltic pump (Cole-Parmer, Vernon Hills, IL, USA), a dip-in conductivity probe (eDaq, Colorado Spring, CO, USA), and a temperature-controlled water bath (Cole-Parmer, Vernon Hills, IL, USA).

3.2. Membrane fabrication

Silica nanoparticles (SiNPs) were chosen as a base material for the porous, hydrophobic layer due to their relatively high thermal conductivity (~ 1.4 W m^{-1} K^{-1}), low cost, and wide range of possible sizes. The nearly spherical shape of SiNPs also allows us to easily approximate the constructed hydrophobic layer properties (e.g., porosity) and enables simplified modeling of gas transport.

To secure the negatively charged SiNPs on the PCTE membrane, PEI, a positively charged polyelectrolyte, was first grafted onto the membrane using the dopamine-assisted direct grafting method reported in our recent publication [32] (Fig. 2). The abundant catechol groups of poly(dopamine) (PDA) react with the amine groups of PEI via Michael addition or the Schiff base reaction [33,34], enabling the direct grafting of PEI onto a PDA-coated substrate. Briefly, 50 mM of aqueous Tris buffer was prepared with the pH adjusted to 8.5 by adding appropriate amount of 1 M HCl. In the meantime, 100 mg of dopamine hydrochloride was dissolved in 80 mL of DI water, followed by the addition of 20 mL of the Tris buffer. After vigorous mixing for ~ 10 s, the solution was poured into a glass Petri dish containing PCTE membranes, which initiates the PDA coating on the membranes. The Petri dish wrapped with aluminum foil was left on a shaker platform for 30 min. Then, the membranes were gently rinsed with DI water multiple times to remove any residual reagents. For PEI grafting, the membranes were immersed in an aqueous PEI solution (10 g/L) for 4 h. After rinsing with DI water, the membranes were stored in DI water at 4 °C until further modification.

To construct a thin hydrophobic layer, vacuum filtration of a SiNP
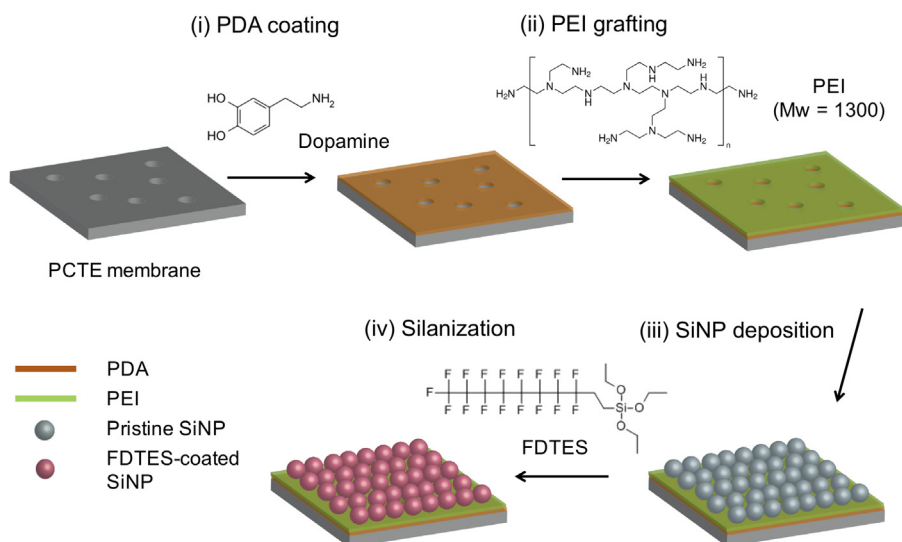
Fig. 2. Schematic diagram of membrane modification procedure. (i) A thin layer of polydopamine (PDA) is formed on a polycarbonate track-etched (PCTE) membrane in aqueous Tris-buffer solution at pH 8.5. (ii) Polyethyleneimine (PEI) is grafted onto PDA via Michael addition/Schiff base reaction. (iii) Silica nanoparticles (SiNPs) are deposited on the membrane by vacuum filtration of a SiNP suspension prepared in 1 mM NaCl aqueous solution (0.01 wt%). (iv) Surface of SiNPs is fluorinated by coating with perfluorodecyltriethoxysilane (FDTES).

suspension solution was performed through the PEI modified PCTE membranes. The as-received SiNP solution (from Nanocomposix, Inc., 10 mg/mL) was diluted with 1 mM NaCl to a final SiNP concentration of 0.01 wt%. To prevent bacterial growth, a small amount of sodium azide was added (0.01 wt%). We performed image analysis to estimate the size of SiNPs by taking more than five SEM micrographs of SiNPs dispersed on a silicon wafer. The average radius ($\bar{a}$) was estimated to be 52.4 ± 2.9 nm, much larger than the pore radius of PCTE membranes (approximately 25 nm). The effective area of the PCTE membrane mounted on the vacuum filtration unit was 2.01 cm². After a SiNP suspension of an appropriate volume was filtered through the PEI-modified membrane, the membrane was removed and air-dried for 24 h. For hydrophobic surface modification of the deposited SiNPs, the membrane was immersed in a solution of FDTES (0.4% v/v) in hexane overnight. The silanization reaction was completed by drying the membranes on a hot plate at 80 °C for 24 h.

3.3. Estimation of the SiNP layer porosity

Estimating the porosity of the hydrophobic layer is important to determine its permeability for water vapor. We estimated the porosity of the SiNP layers by employing the Kozeny-Carman equation, which correlates the porosity of a porous medium (in this work, SiNP layer) with a characteristic length (e.g., particle radius) and flow velocity under a hydraulic pressure. To reliably measure the porosity, we filtered a large volume (30 mL) of the SiNP suspension through a PCTE membrane, resulting in the formation of a SiNP layer approximately 11 μm in thickness (Supplementary Data S3 and Fig. S4). Based on the difference between flow velocities through SiNP-deposited membranes and pristine membranes, the hydraulic resistance of the SiNP layer and corresponding hydraulic pressure drops were calculated. Detailed experimental procedure and calculations are shown in Supplementary Data S3. After incorporating the experimentally determined values and solving the Kozeny-Carman equation by the Newton-Raphson iterative method, the porosity of the SiNP layers was obtained as 0.39 ± 0.03, which is close to the porosity of randomly packed spheres, 0.36 [35].

3.4. Determination of urea concentration

Urea rejection of the developed membranes was assessed in OD experiments using 0.3 M urea and 3 M NaCl as feed and draw solutions, respectively. We used a colorimetric method to determine the urea concentration in the draw solution after OD experiments and calculate the rate of urea permeation through the membrane. We adapted the most recent protocol developed by Chen and Li [36], suitable for urea detection down to trace levels (< 100 nmol L⁻¹). The detailed procedure for the urea concentration estimation using UV–vis spectroscopy is referred to Supplementary Data S6.

4. Results and discussion

4.1. Properties of the hydrophobic SiNP layer

To achieve fast water transport and a high selectivity with the fabricated membranes, it is critical to create a thin and robust hydrophobic SiNP layer while simultaneously maintaining the hydrophilicity of the underlying PCTE membrane. The SiNP layer is formed by vacuum filtration of a nanoparticle suspension onto the membrane surface, and the SiNP layer thickness can be easily tuned by adjusting the volume and concentration of the filtered SiNP suspension. Modifying the PCTE base membrane with PEI contributes to stable SiNP layer formation via electrostatic attraction between the positively charged PEI and negatively charged SiNPs (Supplementary Data S1 and Fig. S2). Fig. 3a–d shows cross-sectional images of the SiNP layers after filtration of different volumes of SiNP suspension. As expected, the SiNP layer thickness increases with a larger volume of the SiNP suspension (Fig. 3e), indicating that the SiNP layer thickness can be readily controlled by changing the SiNP suspension volume. We quantify thickness of the SiNP layer using the normalized thickness, which is defined as the layer thickness (l) divided by the average SiNP radius ($\bar{a}$), i.e., normalized thickness = $l/\bar{a}$. As discussed in Section 2.1, the ratio of the hydrophobic layer thickness (l) to the effective pore radius (a_{eff}) is a determining factor for water flux driven by Knudsen diffusion. For a network of perfect spheres with a porosity of ε, a_{eff} is directly proportional to $\bar{a}$, i.e., $a_{eff} = \frac{2\varepsilon}{3(1-\varepsilon)}\bar{a}$ [37,38]. Therefore, the normalized thickness ($l/\bar{a}$) can serve as a representative parameter that characterizes the vapor permeability of the SiNP layer.

Coating the SiNP layer with FDTES coating renders the surface superhydrophobic, exhibiting a water contact angle greater than 150°, while the other side of membrane (PCTE) is still hydrophilic, showing a contact angle of 72.3 ± 1.5° (Fig. 3f). This contact angle is moderately higher than that of a pristine PCTE membrane (48.1 ± 1.3°), probably due to physical adsorption of FDTES onto the PCTE membrane. Nevertheless, FDTES modification does not compromise the wettability of the PCTE membrane, and water readily permeates through the membrane pores (Supplementary Data S2 and Fig. S3).

4.2. Demonstration of osmotically driven vapor flow

To demonstrate vapor-phase water transport across the SiNP-PCTE membrane driven by an osmotic pressure difference, we employed a diffusion cell consisting of two reservoirs that contain a DI water feed and an NaCl draw solution (Fig. 4a, Supplementary Data S4 and Fig. S5). The membrane was mounted between the reservoirs with the SiNP
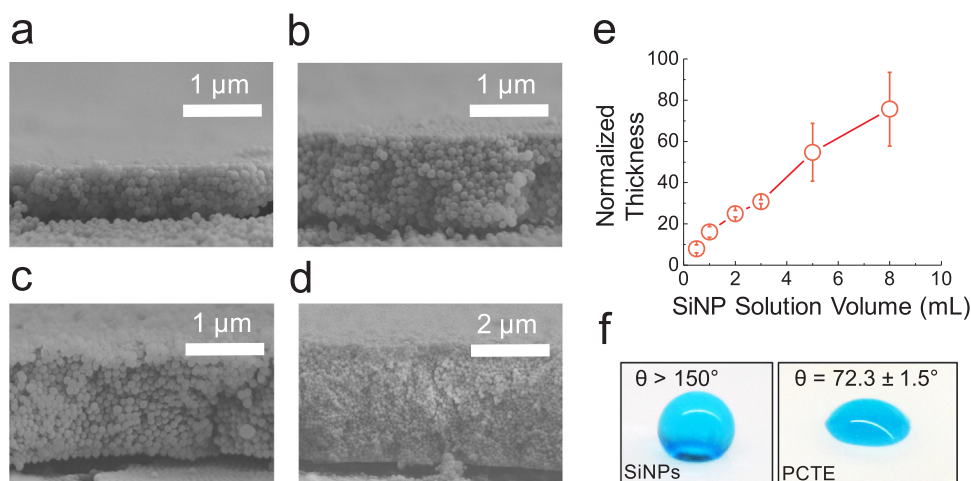
Fig. 3. Characteristics of the SiNP layers. SEM cross-sectional images of SiNP layers formed on PCTE membranes after filtering (a) 1 mL, (b) 2 mL, (c) 3 mL, and (d) 5 mL of SiNP suspension. (e) Normalized thickness (i.e., SiNP layer thickness divided by the average radius of SiNPs) as a function of SiNP suspension solution volume. (f) Images and contact angles (θ) of a water droplet on the SiNP layer (left image) and the PCTE side (right image) of SiNP-PCTE membrane after silanization.
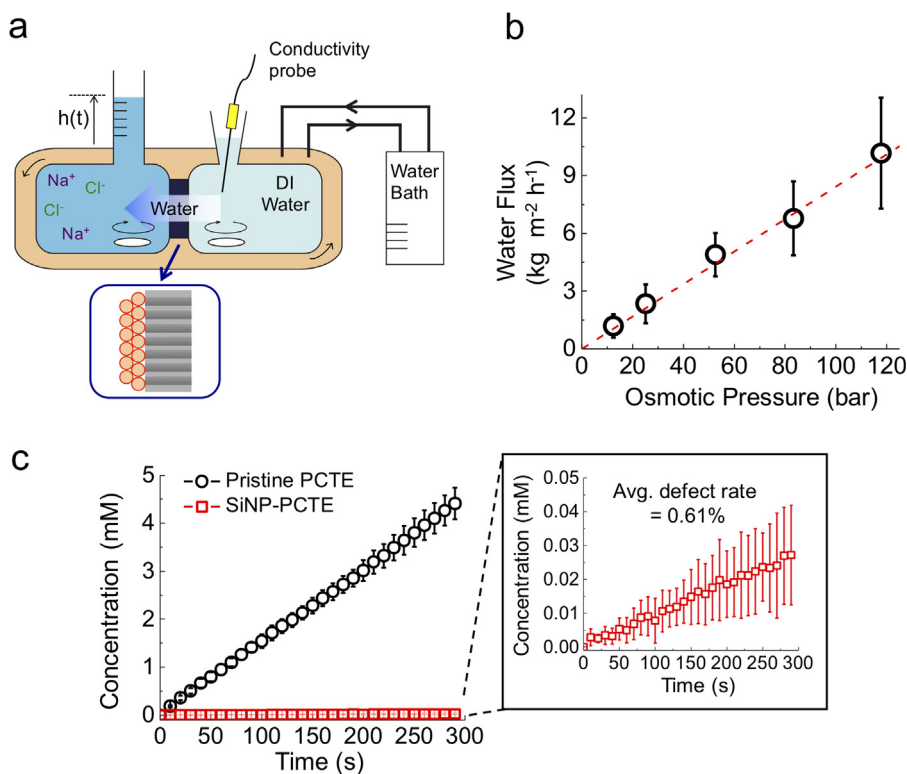
Fig. 4. Characterization of membrane transport properties. (a) Schematic illustration of the diffusion cell with reservoirs containing an NaCl draw solution and a deionized water feed. The membrane is oriented with the SiNP layer facing the draw solution. (b) Mass flux of water vapor through the membrane at various draw solution osmotic pressures corresponding to 0.25, 0.5, 1, 1.5, and 2 M NaCl at 50 °C. Error bars represent standard deviation for three different membranes. The red dashed line is included to guide the eye. (c) Feed solution concentration of NaCl over time for the pristine PCTE and SiNP-PCTE membranes (normalized thickness = 16.1 ± 2.6) at room temperature (25 °C). The draw solution is 1 M NaCl. Error bars represent standard deviation for three different membranes. The estimated defect rate is approximately 0.61%.

layer oriented facing the draw solution to minimize concentration polarization. The temperature of the diffusion cell was maintained constant using a circulating water jacket pumped from an external temperature-controlled bath. Magnetic stir bars were used to maintain uniform bulk concentration and minimize concentration polarization. A glass syringe with graduated volumes was connected to the draw solution reservoir to measure temporal volume increase of the draw solution by water flux and a conductivity probe was employed in the feed reservoir to monitor any solute leakage. Details on the experimental apparatus and procedures are presented in Supplementary Data S4 and Fig. S5.

Fig. 4b shows the measured water flux at 50 °C for different osmotic pressures corresponding to draw solution concentrations of 0.25, 0.5, 1, 1.5, and 2 M NaCl. The water flux linearly increases with escalating osmotic pressure difference, as is expected from Eq. (6) since the partial vapor pressure difference is directly proportional to the osmotic pressure difference. The observed flux behavior therefore indicates that vapor-phase transport through the membrane is occurring. We note that liquid-phase osmotically driven flow across the membrane is not possible, even if the membrane is completed wetted, since the wetted SiNP

layer does not reject salt ions and thus cannot generate an osmotic pressure difference. Our data also demonstrates that the effects of concentration polarization and temperature polarization are minimal, as both phenomena become more detrimental at higher water fluxes and would result in deviation from the observed linear trend.

4.3. Salt rejection and membrane defects

A robust and defect-free hydrophobic membrane is crucial for achieving high water flux and salt rejection. Membrane wetting will result in compromised selectivity since solutes in the feed water can diffuse directly through a wetted membrane. The presence of hydrophilic defects also reduces the effective area of the hydrophobic membrane surface that facilitates vapor transport, reducing the water flux. Furthermore, any leakage of draw solutes through membrane defects aggravates concentration polarization because of the increased salt concentration in the pores of the support PCTE membrane.

We quantified the membrane defects by measuring the rate of salt leakage via diffusion (Supplementary Data S5 and Fig. S6). The feed and draw reservoirs were filled with DI water and 1 M NaCl,
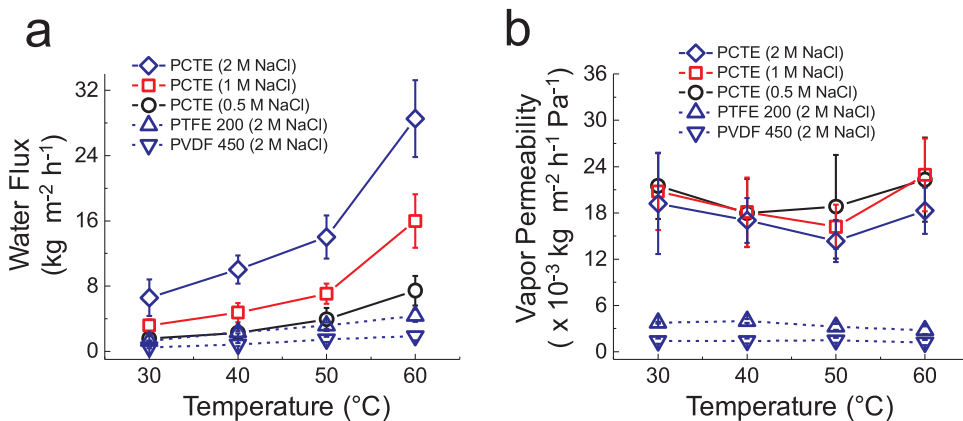
Fig. 5. Transport characteristics of SiNP-PCTE membranes (normalized thickness = 16.1 ± 2.6) and commercial hydrophobic membranes (i.e., PTFE 200 and PVDF 450). (a) Mass flux of water vapor and (b) vapor permeability at different temperatures and draw solution concentrations. Error bars represent standard deviations from three different membranes.

respectively, and connected to an external water container using si-phons. Using this setup, any convective flow across the membranes was eliminated, and the increase in salt concentration of the feed was solely due to the diffusion. Fig. 4c shows the temporal changes of salt concentration for SiNP-PCTE membranes (normalized thickness = 16.1 ± 2.6) and pristine PCTE membranes as a control. The salt concentration for pristine PCTE membranes increased rapidly, whereas the SiNP-PCTE membranes demonstrated a salt leakage rate more than two orders of magnitude lower. We define the defect rate R_{defect} as the salt diffusion rate of the SiNP-PCTE membrane divided by that of the pristine PCTE membrane. The diffusion rate was estimated by linear fitting of the temporal salt concentration changes (Supplementary Data S5). With this definition, R_{defect} of unity indicates that the membrane is completely wetted while R_{defect} of 0 means no presence of defects. The average defect rate was 0.0061, indicating a membrane with a near-negligible quantity of defects.

4.4. Water flux and vapor permeability characterization

4.4.1. Impact of temperature on the vapor permeability

The partial vapor pressure difference between the feed and the draw solution is highly dependent on temperature (Eq. (6)). Fig. 5a shows the water flux across the SiNP-PCTE membranes (normalized thickness = 16.1 ± 2.6) for different draw concentrations and temperatures. Consistent with the previously shown water flux dependence on osmotic pressure (Fig. 4b), the measured water flux is higher at increased draw concentrations, and the rate of increase is much greater at the higher temperatures. This strong dependence of water flux on the temperature is expected, as the vapor pressure of pure water exponentially increases with temperature based on Antoine equation [24].

For comparison, we measured the water flux of two commercially available membranes, PTFE 200 and PVDF 450, as representative hydrophobic microporous membranes used in OD and MD applications. Although the two membranes also exhibit higher fluxes at higher temperature, the water flux of SiNP-PCTE membranes is substantially larger than the commercial membranes, showing the superior membrane performance. We also note that the water flux of SiNP-PCTE membranes at relatively high temperatures may be comparable to that which can be obtained by common TFC membranes using the same draw solution concentration. For example, if we compute the water flux per given osmotic pressure difference as a simplified estimate of the permeability, the values are approximately ∼ 0.16 L m^{-2} h^{-1} bar^{-1} at 50 °C and ∼ 0.30 L m^{-2} h^{-1} bar^{-1} at 60 °C, which are mildly lower than the water permeability coefficient of typical TFC membranes (∼ 1 L m^{-2} h^{-1} bar^{-1}) [29,31,39]. Construction of SiNP layer with a smaller thickness will result in further increases in water flux, comparable to that of TFC-FO membranes, as we will discuss further in the following subsection.

Fig. 5b shows the vapor permeability (A_v) calculated from each case
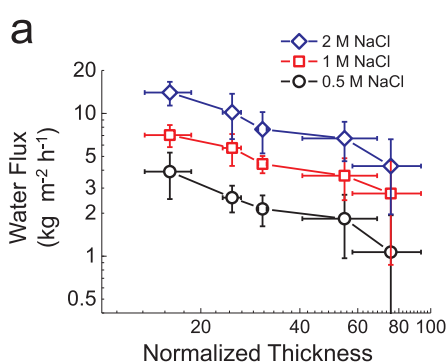
of the water flux measurement ($A_v = J_w (p_F - p_D)^{-1}$, Eq. (4)). The vapor permeabilities of each membrane (i.e., the SiNP-PCTE, PTFE 200, and PVDF 450) show consistent values for different temperatures and draw concentrations, as we found theoretically in Section 2.2. The SiNP-PCTE membrane demonstrated 1 – 2 orders of magnitude higher vapor permeability than the commercial PTFE and PVDF membranes, indicating the superior water transport properties of the developed membranes.

4.4.2. Effect of SiNP layer thickness on vapor permeability

The hydrophobic layer thickness of the SiNP-PCTE membrane will strongly impact the water flux and vapor permeability. Fig. 6a shows the water flux for SiNP-PCTE membranes with different normalized thicknesses and draw concentrations at a given temperature (50 °C). The thicker SiNP layer (i.e., larger normalized thickness) creates an increased diffusion path and therefore imposes larger transport resistances, resulting in a reduced water vapor flux.

The vapor permeabilities that correspond to each water flux measurement are shown in Fig. 6b. For a given normalized thickness, the vapor permeabilities at different draw concentrations are in good agreement, re-emphasizing that the permeability is an intrinsic transport property for membranes. The vapor permeability decreases as normalized thickness increases with an approximate slope of − 1 in log-log scale (triangle in Fig. 6a), in agreement with the expectation that the dominant transport mechanism is diffusion. To allow for comparison, the vapor permeabilities of the two commercial membranes (PTFE 200 and PVDF 450) as well as values found in the literature (Table 1) are also shown. Generally, the permeability values for the SiNP-PCTE membrane at the smallest thickness are around an order of magnitude higher than comparable values in the literature.

Although the higher flux observed with the SiNP-PCTE membrane can largely be attributed to the reduced thickness of the vapor gap, the increased thermal conductivity of the SiNP layer is also advantageous. OD and MD typically employ highly porous, polymeric membranes. While a high porosity can reduce the diffusion resistance, the increased fraction of air also reduces the effective thermal conductivity of the membrane, which leads to more severe temperature polarization in OD. On the other hand, metal oxides such as silica have a higher thermal conductivity than polymer materials, allowing for partial alleviation of temperature polarization. Although there is little room for modifying porosity, the ability to easily tune the thickness of SiNP layer by vacuum filtration enables fabrication of membranes of significantly higher vapor permeability compared to typically available microporous hydrophobic membranes (Fig. 6b).

The expected vapor permeability of SiNP-PCTE membrane from Eq. (4) is shown in Fig. 6b based on the experimentally determined structural parameters (i.e., $\varepsilon = 0.39$, $\tau = 1.6$, and $\bar{a} = 52.4$ nm). The tortuosity factor τ was determined using Bruggeman correlation (i.e., $\tau = \varepsilon^{-1/2}$) [40] and was consistent with values in literature for a network of randomly packed perfect spheres which range between 1.4 and
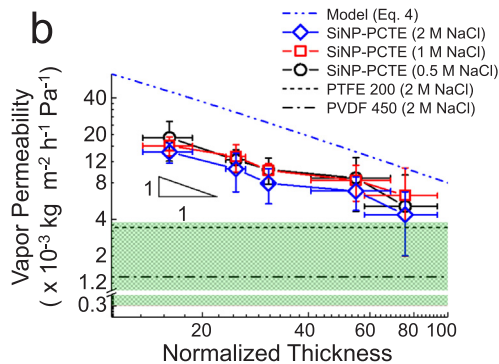
Fig. 6. Water transport properties of SiNP-PCTE membranes. (a) Mass flux of water vapor and (b) vapor permeability for different normalized thicknesses and draw solution concentrations. The temperature of the NaCl draw solution and deionized water feed during the experiments was fixed at 50 °C. Error bars represent standard deviations from three different membranes. In (b), vapor permeabilities of commercial membranes (black dashed lines) and those reported in literature (shaded area, Table 1) are also provided for comparison. The triangle shows a slope of − 1 in log-log scale, indicating diffusion-dominant flow across the SiNP-PCTE membranes (i.e., vapor permeability ∝ normalized thickness^{-1}). The blue dashed line shows vapor permeability estimated from Eq. (4) with porosity of 0.39 and tortuosity factor of 1.6, assuming that the SiNP layer is a randomly packed network of perfect spheres.

Table 1
Vapor permeabilities of osmotic distillation membranes reported in literature and current work.

Ref.	Membrane material	Draw solute	Temperature	Vapor permeability[a] ($\times 10^{-3}$ kg m^{-2} h^{-1} Pa^{-1})
Mengual et al. [10]	Polytetrafluoroethylene	NaCl	40 °C	~ 0.27
Godino et al. [11]	Polytetrafluoroethylene	NaCl	30–50 °C	2.66–2.97
Gostoli et al. [12]	Polypropylene	NaCl	25–50 °C	1.16–1.30
Courel et al. [14]	Polytetrafluoroethylene	CaCl$_2$	25 °C	~ 2.17
Warczok et al. [15]	Polytetrafluoroethylene	NaCl, CaCl$_2$	35 °C	0.76–3.79
Current work	Silicon dioxide	NaCl	30–60 °C	14.4–22.3

[a] Vapor permeability is defined as the mass flux of water divided by the partial vapor pressure difference (unit: kg m^{-2} h^{-1} Pa^{-1}). The vapor permeabilities from current work shown in this table correspond to membranes with a normalized thickness of 16.1 $\pm$ 2.6 (see Fig. 5).

1.6 [41,42]. Detailed calculations of the vapor permeability are presented in Appendices A and C. Both the theoretical and experimentally determined values of the vapor permeability, A_v, show an inverse proportionality with the normalized thickness. However, the experimental values of A_v are substantially lower than the theoretical predictions. We suspect that this is due to the relatively low surface porosity of PCTE membrane (i.e., ~ 5%), which may make it difficult to realize complete wetting of the PCTE membrane surface in contact with hydrophobic SiNPs. Nevertheless, this theoretical value can serve as an upper limit of vapor permeability expected from the current nanoparticle layer. Membranes with further reduced SiNP layer thickness are expected to exhibit even higher vapor permeability according to the inverse relation of the vapor permeability and normalized thickness (i.e., $A_v \propto$ normalized thickness^{-1}).

We note that the relation between vapor permeability and normalized thickness holds only when the diffusion resistance is dominant compared to the transport resistances associated with evaporation and condensation [17,18]. As the SiNP layer thickness decreases, a ballistic transport of water molecules across the vapor gap can occur without colliding with the SiNP surface, and the transport resistances at the liquid/vapor interfaces also become important. In such cases, the water flux would approach a finite, maximum value until the wetting of the membrane becomes energetically favorable at a sufficiently thin SiNP layer thickness [17,43,44]. Nevertheless, the attainable water flux through a membrane with the thin layer is comparable to commercially available FO membranes.

4.5. Rejection of small and neutrally charged molecules

Poor rejection of small, uncharged species such as boron and urea remains a challenge for TFC membranes [4–6,45]. Liquid/vapor interfaces can provide an effective barrier for these contaminants due to their low vapor pressures [46,47]. We performed OD experiments with SiNP-PCTE membranes using urea as a small, neutrally charged model contaminant in the feed. Commercially available TFC-FO membranes were used as a benchmark. The same experimental setup used for vapor permeability measurement in the previous subsections was employed except that the hydrophobic SiNP layer or the salt-rejecting active layer of the TFC membrane was oriented facing the feed solution. The feed and draw solutions used were 0.3 M urea and 3 M NaCl, respectively. To investigate temperature effects on the rejection performance, the experiments were conducted at two different temperatures, 25 °C and 50 °C, with three different samples taken for each type of membrane at each temperature. For TFC membranes, the draw solutions were collected after approximately 50 μL of permeate flow was obtained. For SiNP-PCTE membranes, on the other hand, the draw solutions were collected after approximately 15 μL and 50 μL of draw solutions were withdrawn at 25 °C and 50 °C, respectively, due to the slower vapor transport at the lower temperature.

The urea rejection performance was assessed by obtaining a urea permeability coefficient (B_{urea}), analogous to the salt permeability coefficient for TFC-FO membranes [29], defined such that:

$$N_{urea} \equiv B_{urea} \Delta C_{urea}, \tag{7}$$

where N_{urea} and ΔC_{urea} are molar flux of urea and urea solution concentration difference across the membrane, respectively. Due to the negligible concentration polarization effect expected on the feed side of the membrane (Section 4.2), we assume ΔC_{urea} to be the same as the bulk concentration difference (i.e., 0.3 M). As described in Section 3.4, we used a colorimetric method followed by UV–vis spectroscopy to determine the urea concentration in the draw solution (see Supplementary Data S6 and Fig. S7 for adsorption spectra). N_{urea} was then calculated from the increase in urea concentration in the draw solution divided by the OD experiment time period and used to obtain the value of B_{urea}.

Fig. 7 shows the urea permeability coefficients for the TFC-FO membrane and the SiNP-PCTE membrane (normalized thickness = 24.9 $\pm$ 1.6) at 25 °C and 50 °C. The values of B_{urea} for TFC-FO membranes range from 1.0×10^{-5} m s^{-1} (33.9 L m^{-2} h^{-1}) at 25 °C to 2.2×10^{-5} m s^{-1} (80.8 L m^{-2} h^{-1}) at 50 °C, which are significantly larger than a typical salt (NaCl) permeability coefficient of TFC-FO membranes of ~ 2.8×10^{-7} m s^{-1} (~ 1 L m^{-2} h^{-1}) [29,31,39]. This high urea permeation is consistent with the poor urea rejection reported in the literature [4], which only worsens as temperature increases due to the increased solute diffusivity at higher temperatures [48,49].

Urea permeation through SiNP-PCTE membranes is 2–3 orders of magnitude lower than that of TFC-FO membranes, with values of B_{urea} ranging from 1.3×10^{-8} m s^{-1} (0.45×10^{-1} L m^{-2} h^{-1}) at 25 °C to 8.8×10^{-8} mm s^{-1} (3.2×10^{-1} L m^{-2} h^{-1}) at 50 °C. The significantly lower urea permeation is attributed to the effective barrier imposed by the liquid/vapor interfaces. The higher B_{urea} at 50 °C compared to 25 °C
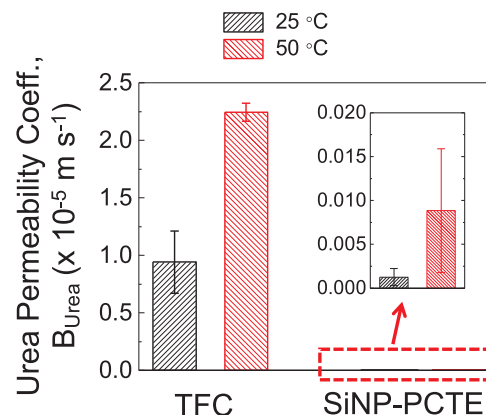
Fig. 7. Urea permeability coefficients ($B_{urea} = N_{urea}/\Delta C_{urea}$) of commercially available thin-film composite (TFC) FO membranes and SiNP-PCTE membranes (normalized thickness = 24.9 $\pm$ 1.6). Urea rejection experiments were performed for three samples of each type of membrane at 25 °C and 50 °C. Error bars represent standard deviations. The urea flux was estimated from the increase of urea concentration in the draw solution (3 M NaCl). The concentration of urea in the draw solution was measured by UV–vis spectrophotometer (see Supplementary Data S6 and Fig. S7). The inset is a magnified view of the urea permeability coefficients of the SiNP-PCTE membranes.

may be attributed to the leakage through defects with an increased diffusivity of urea. Nevertheless, the excellent urea rejection shows the promise of the developed membrane for treating water sources contaminated by neutrally charged, low weight molecules.

5. Conclusion

In this work, we developed a highly selective and permeable osmosis membrane by constructing a thin, hydrophobic SiNP layer with tunable thickness on a hydrophilic porous support. The water flux behavior as well as the high salt rejection verified that water transport across the membrane occurs in the vapor phase. We calculated the intrinsic membrane vapor permeability from the osmotic flow measurements for different draw solution concentrations, temperatures, and SiNP layer thicknesses. The obtained vapor permeability was in reasonable agreement with the vapor permeability predicted from the dusty-gas model and was about 1–2 orders of magnitude higher than that of hydrophobic membranes reported in the literature. While the

osmotic water flux across the membrane was mildly lower than a commercial TFC-FO membrane, the observed and theoretically predicted thickness dependence of vapor permeability suggests that further reductions in the SiNP layer thickness will result in comparable water fluxes to TFC-FO membranes. Finally, the developed membrane exhibited approximately 2–3 orders of magnitude lower permeation of urea, a representative small, neutrally charged molecule, than the TFC membrane. Overall, the nanostructured vapor-gap osmosis membrane has great potential to provide high-purity permeate water without the high energy requirements of conventional thermal separation processes. These properties can substantially improve the efficiency and utility of osmotic membrane processes.

Appendix A. Derivation of the vapor permeability (A_v)

As shown in Eq. (1), the dusty-gas model in the frame of the Stefan-Maxwell equation can be formulated as follows:

$$\sum_{j=1,j\neq i}^{n} \frac{x_j N_i - x_i N_j}{D_{ij}^e} + \frac{N_i}{D_{iM}^e} = -\frac{p_t}{R_g T}\nabla x_i - \frac{x_i}{R_g T}\left(1 + \frac{B_0 p_t}{\eta D_{iM}^e}\right)\nabla p_t. \tag{A1}$$

The definitions of the variables in this equation and other parts of the appendices are provided in the Nomenclature. The viscous permeability B_0 is defined such that $\bar{u}\equiv-(B_0/\eta)\nabla p_t$ where $\bar{u}$ is the average velocity of the gas mixture incurred by the total pressure gradient. The Knudsen diffusion coefficient D_{iM} for a long capillary with a radius of a is given as $D_{iM} = (2/3)a\bar{v}_i$ where $\bar{v}_i$ is a mean velocity of gas species i. For a binary mixture of water vapor and air, the Eq. (A1) can be simplified to:

$$\frac{x_a N_w - x_w N_a}{D_{wa}^e} + \frac{N_w}{D_{wM}^e} = -\frac{\nabla p_w}{R_g T} - \frac{B_0 p_w}{\eta D_{wM}^e R_g T}\nabla p_t, \tag{A2}$$

where the subscripts w and a stand for water vapor and air, respectively, and $p_t \nabla x_w + x_w \nabla p_t = \nabla(p_t x_w) = \nabla p_w$ is applied.

The last term indicates the contribution from the viscous flow driven by the total pressure gradient. For a transport medium comprising cylindrical tubes, B_0 is given as $B_0 = \varepsilon a^2/8$ with tube radius a. For porous media comprising perfect spheres, an effective pore radius a_{eff} can be deduced from the relation $a_{eff} = \frac{2\bar{a}\varepsilon}{3(1-\varepsilon)}$, where $\bar{a}$ is the average radius of spheres ($\bar{a} = 52.4 \pm 2.9$ nm in this work) and ε is the porosity [37,38]. As we show in Supplementary Data Section S3, the average porosity of the SiNP layer was determined to be 0.39. Based on the effective pore radius, D_{wM}^e can be obtained as $D_{wM}^e = \left(\frac{2\varepsilon}{3\tau}\right)a_{eff}\bar{v}_w$ [37,38]. The tortuosity factor τ was determined to be 1.6 using Bruggeman correlation (i.e., $\tau = \varepsilon^{-1/2}$) [40]. This value is consistent with those in the literature for a porous network consisting of spheres, ranging between 1.4 and 1.6 [41,42]. The mean velocity of water vapor molecule is $\bar{v}_w = \sqrt{\frac{8R_g T}{\pi M_w}} \sim 600$ m s^{-1} with the molar mass of water, M_w, of 1.8×10^{-2} kg mol^{-1} and at temperature of 25–60 °C. Comparing the water vapor pressure (2–20 kPa for 25–60 °C) to the total pressure ($p_t \sim 1$ bar), we find that air can be regarded as a major species, and therefore, we approximate the viscosity of the gas mixture to be that of air. The relative magnitude of the last to the first term in the right-hand side of Eq. (A2) can be approximated as $\frac{B_0 p_w |\nabla p_t|}{\eta D_{wM}^e |\nabla p_w|}$. As air in the SiNP layer is assumed to be stagnant and the partial vapor pressure gradient can be partially counter-balanced by the partial pressure gradient of air, it is expected that $\frac{|\nabla p_t|}{|\nabla p_w|} = \frac{|\nabla (p_w + p_a)|}{|\nabla p_w|} \leq 1$. With $\varepsilon \sim 0.39$, $\tau \sim 1.6$, $\bar{a} \sim 50$ nm, $\bar{v}_w \sim 600$ m s^{-1}, $p_w \sim 10$ kPa, and $\eta \sim 1.8 \times 10^{-5}$ Pa s, we find $\frac{B_0 p_w |\nabla p_t|}{\eta D_{wM}^e |\nabla p_w|} \leq \frac{B_0 p_w}{\eta D_{wM}^e} \sim 0.006 << 1$, showing that the momentum contribution by viscous flow is negligible. Then, Eqs. (1), (A1) or (A2) can be simplified as follows:

$$\frac{x_a N_w - x_w N_a}{D_{wa}^e} + \frac{N_w}{D_{wM}^e} = -\frac{\nabla p_w}{R_g T}. \tag{A3}$$

Due to the small solubility of air in water, we assume that air in the SiNP layer is stagnant (i.e., $N_a = 0$). Noting that $x_a + x_w = 1$, $x_w = p_w/p_t$, and $x_a = p_a/p_t$ where p_w and p_a are the partial pressures of water vapor and air, respectively, we reach the following Equation:

$$-\frac{dp_w}{dz}\frac{1}{R_g T} = \frac{\tau N_w}{\varepsilon D_{wa}}\left[1 + \alpha - \frac{p_w}{p_t}\right], \tag{A4}$$

where $\alpha = D_{wa}/D_{wM}$. Further assuming a nearly uniform total pressure of 1 bar and integrating the above Equation with respect to p_w using boundary conditions of $p_w = p_D$ at $z = 0$ and $p_w = p_F$ at $z = l$ leads to [28]:

$$N_w = \frac{\varepsilon D_{wa} p_t}{\tau R_g T l}ln\left[\frac{1 - \frac{p_F}{(1+\alpha)p_t}}{1 - \frac{p_D}{(1+\alpha)p_t}}\right], \tag{A5}$$

where p_D and p_F are the partial pressures of water vapor at the draw and feed solution sides, respectively. Using Taylor expansion, the above equation can be approximated to the following equation:

$$N_w = -\frac{\varepsilon D_{wa} p_t}{\tau R_g T l}\left[\frac{x_F - x_D}{1+\alpha} + \frac{(x_F - x_D)(x_F + x_D)}{2(1+\alpha)^2} + O(x_F^3) + O(x_D^3)\right].$$

(A6)

Note that x_F and $x_D \sim O(0.01\text{–}0.1)$. Considering that the mean free path (λ) of approximately 100 nm at an ambient pressure and the effective pore size $a_{eff} \sim 20$ nm, the effective Knudsen number ($Kn = \lambda/a_{eff}$) is $O(1\text{–}10)$. In this transition regime, which is the transport regime between the Knudsen dominant regime ($Kn >> 10$) and the molecular diffusion regime ($Kn << 1$), it is expected that $\alpha \sim O(1)$. Therefore, neglecting the second order and higher order terms does not result in a significant error. The following equation for mass flux, J_w, can then be reached:

$$J_w = M_w|N_w| = \frac{\varepsilon D_{wa}}{\tau R_g T l(1+\alpha)}(p_F - p_D).$$

(A7)

And we finally reach the expression for the vapor permeability (Eq. (4)) as following:

$$A_v = \frac{J_w}{p_F - p_D} = \frac{\varepsilon D_{wa} M_w}{\tau R_g T l(1+\alpha)}.$$

(A8)

Assuming that the SiNP layer is a structure of randomly packed perfect spheres and using the structural parameters (ε, τ, $\bar{a}$ and l), an expected value of A_v can be obtained using the Knudsen and molecular diffusion coefficients as shown in Appendix C.

Further examination of Eq. (A8) reveals the structural dependency of the vapor permeability coefficient. The Knudsen diffusion coefficient (D_{wM}) is proportional to effective pore radius (a_{eff}), and therefore to $\bar{a}$, i.e., $D_{wM} = \frac{2\bar{v}_w}{3}a_{eff} = \frac{4\varepsilon\bar{v}_w}{9(1-\varepsilon)}\bar{a}$. On the other hand, the molecular diffusion coefficient (D_{wa}) is independent of pore geometry (see Appendix C). As a result, α ($= D_{wa}/D_{wM}$) is inversely proportional to a_{eff} (and therefore to $\bar{a}$). For large a_{eff} ($\alpha << 1$), molecular diffusion is the dominant vapor transport mechanism. From Eq. (A8), we note $A_v \cong \frac{\varepsilon D_{wa} M_w}{\tau R_g T l}$, indicating that A_v and therefore J_w, become inversely proportional to the SiNP layer thickness (l), i.e., $A_v \propto l^{-1}$, and independent of a_{eff}. For small a_{eff} ($\alpha >> 1$), on the other hand, Knudsen diffusion is the dominant mechanism for the vapor transport. Noting again that $\alpha = D_{wa}/D_{wM}$, it leads to $A_v \cong \frac{\varepsilon D_{wa} M_w}{\tau R_g T l \alpha} = \frac{2\varepsilon M_w \bar{v}_w}{3\tau R_g T}\left(\frac{l}{a_{eff}}\right)^{-1} = \frac{4\varepsilon^2 M_w \bar{v}_w}{9(1-\varepsilon)\tau R_g T}\left(\frac{l}{\bar{a}}\right)^{-1}$. In this case, A_v and J_w are inversely proportional to the ratio of the membrane thickness to the effective pore radius, i.e., $A_v \propto (l/a_{eff})^{-1} \propto (l/\bar{a})^{-1}$.

Appendix B. Temperature change induced by vapor transport

In osmotic distillation, evaporation of water at the feed-membrane interface takes latent heat from the feed solution, and condensation of water at the draw-membrane interface provides the latent heat to the draw solution. Additionally, any temperature difference between the two interfaces incurs thermal conduction through the membrane material. As a result, a steady state temperature difference is established to balance the two heat transfer modes. A simple scaling analysis for the heat transfer allows us to estimate the temperature difference as following:

$$J_w \Delta L \sim k_{eff}\frac{\Delta T}{l},$$

(A9)

where J_w is mass flux of water vapor, ΔL is the latent heat of water (2.26×10^6 J kg^{-1}), k_{eff} is an effective thermal conductivity of the membrane (i.e., SiNP layer in our study), ΔT is the temperature difference across the membrane with the thickness of l. The effective thermal conductivities of a network of randomly distributed spheres with different porosities were obtained by Argento and Bouvard [50]. For our estimated porosity of 0.39 (see Supplementary Data Section S3), $k_{eff}/k_s \sim 0.25$ where k_s is the thermal conductivity of silica ($k_s \sim 1.4$ W m^{-1} K^{-1}). Even when using the maximum water flux in our experiments ($J_w \sim 30$ kg m^{-2} h^{-1} for $l \sim 1$ μm), the estimated temperature difference is $\Delta T \sim J_w \Delta L l/k_{eff} \sim 0.05$ °C. As the impact of this small temperature on vapor pressure is minimal, we assume an isothermal condition for our experiments.

Appendix C. Temperature dependence of vapor permeability

Since D_{wa} and D_{wM} are temperature dependent parameters, the vapor permeability (A_v) is expected to vary with temperature (T). To investigate the temperature dependence of A_v, we first examined analytical expressions for the diffusion coefficients. Based on the formulation derived by Chapman and Enskog [51], D_{wa} (m^2 s^{-1}) can be written as following:

$$D_{wa} = \frac{cT^{3/2}}{p_t l_{wa}^2 \Omega_D}\left[\frac{1}{M_w} + \frac{1}{M_a}\right]^{1/2},$$

(A10)

where the constant c is given as 1.883×10^{-22}. l_{wa} is a characteristic length associated with Lennard-Jones 12-6 potential and Ω_D is a collision integral for mass diffusion. The approximate analytical expressions for l_{wa} and Ω_D are available in the literature [51,52]. As shown in Appendix A, D_{wM} is given as:

$$D_{wM} = \frac{2a_{eff}}{3}\left(\frac{8R_g T}{\pi M_w}\right)^{1/2}.$$

(A11)

Substituting Eqs. (A10) and (A11) into Eq. (A8) leads to a full analytical expression for A_v. With $p_t = 10^5$ Pa and $\bar{a} = 52.4$ nm, A_v values at different temperatures normalized by the value at 25 °C ($A_{v,o}$) are shown in Figure S1 in Supplementary Data. For the considered temperature ranges in our experiments (i.e., 25–60 °C), the change in A_v values is less than 1%. This negligible temperature dependency indicates that A_v can be used as an intrinsic membrane property.

Appendix D. Derivation of correlation between partial vapor pressure and osmotic pressure

Under the isothermal condition (i.e., uniform T) and in the absence of applied hydraulic pressure (i.e., $P = 0$), applying a Taylor expansion to Eq. (5) leads to following expression for the partial vapor pressure difference:

$$p_F - p_D \approx p_0(T) \left[\frac{(\Pi_D - \Pi_F)V_m}{R_g T} + \left(\frac{V_m}{R_g T}\right)^2 \frac{\Pi_D^2 - \Pi_F^2}{2} \right] \approx \frac{\Delta\Pi V_m}{R_g T} p_0(T),$$

<div align="right">(A12)</div>

where $\Delta\Pi = \Pi_D - \Pi_F$. Even for $\Delta\Pi = 100$ bar, the maximum error occurred by dropping the second-order term on the right-hand side is 3.6%. Therefore, the partial vapor pressure difference, which the driving force for the water vapor transport, is linearly proportional to the osmotic pressure difference between the feed solution and the draw solution.

Appendix E. Supplementary material

Supplementary data associated with this article can be found in the online version at http://dx.doi.org/10.1016/j.memsci.2018.03.059.

References

[1] M. Elimelech, W.A. Phillip, The future of seawater desalination: energy, technology, and the environment, Science 333 (2011) 712–717.
[2] D.L. Shaffer, J.R. Werber, H. Jaramillo, S.H. Lin, M. Elimelech, Forward osmosis: where are we now? Desalination 356 (2015) 271–284.
[3] S.F. Zhao, L. Zou, C.Y.Y. Tang, D. Mulcahy, Recent developments in forward osmosis: opportunities and challenges, J. Membr. Sci. 396 (2012) 1–21.
[4] S. Lee, R.M. Lueptow, Membrane rejection of nitrogen compounds, Environ. Sci. Technol. 35 (2001) 3008–3018.
[5] N. Misdan, W.J. Lau, A.F. Ismail, Seawater reverse osmosis (SWRO) desalination by thin-film composite membrane – current development, challenges and future prospects, Desalination 287 (2012) 228–237.
[6] J.R. Werber, A. Deshmukh, M. Elimelech, The critical need for increased selectivity, not increased water permeability, for desalination membranes, Environ. Sci. Technol. Lett. 3 (2016) 112–120.
[7] W. Kunz, A. Benhabiles, R. BenAim, Osmotic evaporation through macroporous hydrophobic membranes: a survey of current research and applications, J. Membr. Sci. 121 (1996) 25–36.
[8] N.Y. Yip, M. Elimelech, Performance limiting effects in power generation from salinity gradients by pressure retarded osmosis, Environ. Sci. Technol. 45 (2011) 10273–10282.
[9] J. Wei, X. Liu, C.Q. Qiu, R. Wang, C.Y.Y. Tang, Influence of monomer concentrations on the performance of polyamide-based thin film composite forward osmosis membranes, J. Membr. Sci. 381 (2011) 110–117.
[10] J.I. Mengual, J.M.O. Dezarate, L. Pena, A. Velazquez, Osmotic distillation through porous hydrophobic membranes, J. Membr. Sci. 82 (1993) 129–140.
[11] P. Godino, L. Pena, J.I. Mengual, Membrane distillation: theory and experiments, J. Membr. Sci. 121 (1996) 83–93.
[12] C. Gostoli, Thermal effects in osmotic distillation, J. Membr. Sci. 163 (1999) 75–91.
[13] M. Courel, M. Dornier, J.M. Herry, G.M. Rios, M. Reynes, Effect of operating conditions on water transport during the concentration of sucrose solutions by osmotic distillation, J. Membr. Sci. 170 (2000) 281–289.
[14] M. Courel, M. Dornier, G.M. Rios, M. Reynes, Modelling of water transport in osmotic distillation using asymmetric membrane, J. Membr. Sci. 173 (2000) 107–122.
[15] J. Warczok, M. Gierszewska, W. Kujawski, C. Gueell, Application of osmotic membrane distillation for reconcentration of sugar solutions from osmotic dehydration, Sep. Purif. Technol. 57 (2007) 425–429.
[16] M. Gryta, Osmotic MD and other membrane distillation variants, J. Membr. Sci. 246 (2005) 145–156.
[17] J. Lee, R. Karnik, Desalination of water by vapor-phase transport through hydrophobic nanopores, J. Appl. Phys. 108 (2010).
[18] J. Lee, T. Laoui, R. Karnik, Nanofluidic transport governed by the liquid/vapour interface, Nat. Nanotechnol. 9 (2014) 317–323.
[19] R. Jackson, Transport in porous catalysts, Elsevier Scientific Pub. Co., Distributors for the U.S. and Canada; Elsevier, North-Holland, Amsterdam, New York, 1977.
[20] E.A. Mason, A.P. Malinauskas, Gas Transport in Porous Media: The Dusty-Gas Model, Elsevier, Amsterdam, New York, 1983.
[21] R. Krishna, J.A. Wesselingh, The Maxwell-Stefan approach to mass transfer, Chem. Eng. Sci. 52 (1997) 861–911.
[22] R. Remick, C.J. Geankoplis, Binary diffusion of gases in capillaries in the transition region between Knudsen and molecular diffusion, Ind. Eng. Chem. Fundam. 12 (1973) 214–220.
[23] R. Remick, C.J. Geankoplis, Ternary diffusion of gases in capillaries in the transition region between knudsen and molecular diffusion, Chem. Eng. Sci. 29 (1974) 1447–1455.
[24] K.W. Lawson, D.R. Lloyd, Membrane distillation, J. Membr. Sci. 124 (1997) 1–25.
[25] M. Khayet, Membranes and theoretical modeling of membrane distillation: a review, Adv. Colloid Interface Sci. 164 (2011) 56–88.
[26] A. Deshmukh, C. Boo, V. Karanikola, S. Lin, A.P. Straub, T. Tong, D.M. Warsinger, M. Elimelech, Membrane distillation at the water-energy nexus: limits, opportunities, and challenges, Energy Environ. Sci. (2018).
[27] S.K. Bhatia, M.R. Bonilla, D. Nicholson, Molecular transport in nanopores: a theoretical perspective, Phys. Chem. Chem. Phys. 13 (2011) 15350–15383.

[28] A. Deshmukh, M. Elimelech, Understanding the impact of membrane properties and transport phenomena on the energetic performance of membrane distillation desalination, J. Membr. Sci. 539 (2017) 458–474.
[29] A. Tiraferri, N.Y. Yip, A.P. Straub, S. Romero-Vargas Castrillon, M. Elimelech, A method for the simultaneous determination of transport and structural parameters of forward osmosis membranes, J. Membr. Sci. 444 (2013) 523–538.
[30] H. Wex, F. Stratmann, D. Topping, G. McFiggans, The Kelvin versus the Raoult term in the Kohler equation, J. Atmos. Sci. 65 (2008) 4004–4016.
[31] J. Ren, J.R. McCutcheon, A new commercial thin film composite membrane for forward osmosis, Desalination 343 (2014) 187–193.
[32] T.Z. Tong, S. Zhao, C. Boo, S.M. Hashmi, M. Elimelech, Relating silica scaling in reverse osmosis to membrane surface properties, Environ. Sci. Technol. 51 (2017) 4396–4406.
[33] J. Yang, M.A.C. Stuart, M. Kamperman, Jack of all trades: versatile catechol crosslinking mechanisms, Chem. Soc. Rev. 43 (2014) 8271–8298.
[34] Y. Tian, Y.W. Cao, Y. Wang, W.L. Yang, J.C. Feng, Realizing ultrahigh modulus and high strength of macroscopic graphene oxide papers through crosslinking of Mussel-inspired polymers, Adv. Mater. 25 (2013) 2980–2983.
[35] G.D. Scott, D.M. Kilgour, The density of random close packing of spheres, J. Phys. D: Appl. Phys. 2 (1969) 863.
[36] L. Chen, J. Ma, Y. Huang, M.H. Dai, X.L. Li, Optimization of a colorimetric method to determine trace urea in seawater, Limnol. Oceanogr.-Methods 13 (2015) 303–311.
[37] T. Wright, D.M. Smith, D.L. Stermer, Knudsen diffusion in bidisperse mixtures of uniform spheres, Ind. Eng. Chem. Res. 26 (1987) 1227–1232.
[38] D.G. Huizenga, D.M. Smith, Knudsen diffusion in random assemblages of uniform spheres, Aiche J. 32 (1986) 1–6.
[39] C.H. Liu, J. Lee, J. Ma, M. Elimelech, Antifouling thin-film composite membranes by controlled architecture of zwitterionic polymer brush layer, Environ. Sci. Technol. 51 (2017) 2161–2169.
[40] T.R. Ferguson, M.Z. Bazant, Nonequilibrium thermodynamics of porous electrodes, J. Electrochem. Soc. 159 (2012) A1967–A1985.
[41] A. Bertei, B. Nucci, C. Nicolella, Effective transport properties in random packings of spheres and agglomerates, Chem. Eng. Trans. 32 (2013) 1531–1536.
[42] J.A. Currie, Gaseous diffusion in porous media .2. Dry granular materials, Brit. J. Appl. Phys. 11 (1960) 318–324.
[43] B. Lefevre, A. Saugey, J.L. Barrat, L. Bocquet, E. Charlaix, P.F. Gobin, G. Vigier, Intrusion and extrusion of water in hydrophobic mesopores, J. Chem. Phys. 120 (2004) 4927–4938.
[44] A. Luzar, Activation barrier scaling for the spontaneous evaporation of confined water, J. Phys. Chem. B 108 (2004) 19859–19866.
[45] S. Lee, R.M. Lueptow, Reverse osmosis filtration for space mission wastewater: membrane properties and operating conditions, J. Membr. Sci. 182 (2001) 77–90.
[46] T.Y. Cath, S. Gormly, E.G. Beaudry, M.T. Flynn, V.D. Adams, A.E. Childress, Membrane contactor processes for wastewater reclamation in space Part I. Direct osmotic concentration as pretreatment for reverse osmosis, J. Membr. Sci. 257 (2005) 85–98.
[47] T.Y. Cath, D. Adams, A.E. Childress, Membrane contactor processes for wastewater reclamation in space II. Combined direct osmosis, osmotic distillation, and membrane distillation for treatment of metabolic wastewater, J. Membr. Sci. 257 (2005) 111–119.
[48] M.C.Y. Wong, K. Martinez, G.Z. Ramon, E.M.V. Hoek, Impacts of operating conditions and solution chemistry on osmotic membrane structure and performance, Desalination 287 (2012) 340–349.
[49] M. Xie, W.E. Price, L.D. Nghiem, M. Elimelech, Effects of feed and draw solution temperature and transmembrane temperature difference on the rejection of trace organic contaminants by forward osmosis, J. Membr. Sci. 438 (2013) 57–64.
[50] C. Argento, D. Bouvard, Modeling the effective thermal conductivity of random packing of spheres through densification, Int. J. Heat Mass Trans. 39 (1996) 1343–1350.
[51] B.E. Poling, J.M. Prausnitz, J.P. O'Connell, The Properties of Gases and Liquids, 5th ed, McGraw-Hill, New York, 2001.
[52] R.H. Perry, D.W. Green, Perry's Chemical Engineers' Handbook, 8th ed, McGraw-Hill, New York, 2008.